10.1071/WF24067
International Journal of Wildland Fire

Supplementary Material

Pixels to pyrometrics: UAS-derived infrared imagery to evaluate and monitor prescribed fire behaviour and effects

Leo O'Neill[A], *Peter Z Fulé*[A,*], *Adam Watts*[B], *Chris Moran*[C], *Bryce Hopkins*[D], *Eric Rowell*[E], *Andrea Thode*[A] and *Fatemeh Afghah*[D]

[A]School of Forestry, Northern Arizona University, 200 E Pine Knoll Drive, Flagstaff, AZ 86011, USA

[B]Pacific Wildland Fire Sciences Laboratory, U.S. Forest Service, Seattle, WA 98103, USA

[C]National Center for Landscape Fire Analysis, University of Montana, 32 Campus Drive, CHCP 428, Missoula, MT 59812, USA

[D]Holcombe Department of Electrical and Computer Engineering, Clemson University, Clemson, SC 29631, USA

[E]Department of Atmospheric Science, Desert Research Institute, Reno, NV 89512, USA

*Correspondence to: Email: Pete.Fule@nau.edu

Supplementary Material

This document contains supplementary material on the calibration, stabilization, and georectification of thermal images (S1), objectives from each prescribed fire (S2 – S4), and ocular estimates of fire behavior from attending fire researchers (S5).

S1: Thermal imagery pre-processing methods

We used a blackbody calibration source to convert the 16-bit digital numbers to temperature in degrees Celsius. The 16-bit pixel values ranged from 2,800 for the cold regions of the frame to 6,000 for intense flaming areas. We chose not to use Autel's proprietary conversion software because it used the compressed .jpeg thermal images and had no batch processing functionality. Instead, we used a blackbody calibration source to develop an algorithm to convert the thermal imagery from the uncompressed .tiff images. Using the blackbody, we tested the thermal camera using the full range of the calibrator: between 0°–100° Celsius at 5-degree increments (Fig. S1). The results of this bench testing confirmed the accuracy of the radiometric IR sensor and were used to develop a linear conversion algorithm:

Equation S1

$$f(x) = 0.0982x - 268.39$$

where x is the IR sensor's reported digital number and $f(x)$ is the calibrator temperature, which explained the relationship well ($R^2 = 0.99$). We applied this equation to convert the .tiff pixel digital numbers to calibrated temperature.

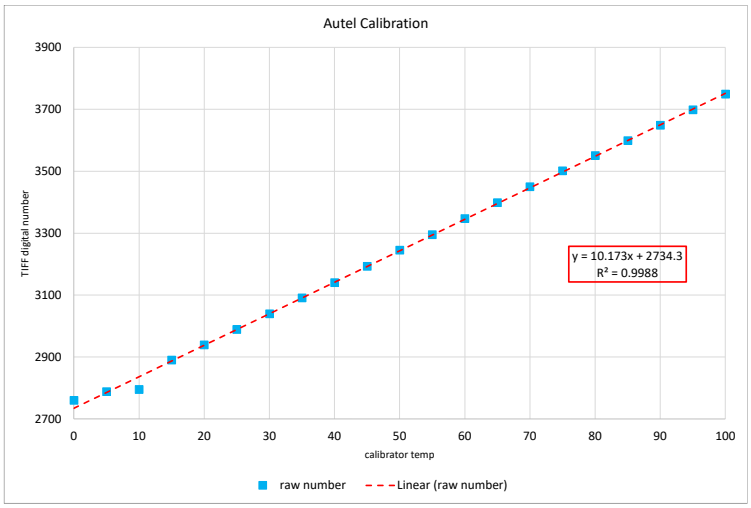

Figure S1: Black body calibration of the IR sensor. UAS was positioned ~2 m away from the black body. Temperatures were recorded from the blackbody setting and the average digital number was derived from the UAS IR raster. The maximum temperature of the blackbody was 100 degrees Celsius, so we were unable to assess the performance of the sensor at higher temperatures.

Next, we stabilized the imagery to coregister each image so that drift such as positional and rotational movement are removed. The process of orthorectifying thermal imagery of fire is challenging, and research to provide an open-source solution is ongoing (Moran *et al.* 2019; Valero *et al.* 2021; Paugam *et al.* 2021). We used OpenCV (Bradski 2000) and Python to test four transformation algorithms and the use of a fire mask to stabilize the thermal image stacks. The models we selected for testing have been used to coregister images for this type of application or were demonstrated to outperform a model previously tested for this application (Mahesh and Subramanyam 2012; Valero *et al.* 2021). We tested: KAZE, Scale-Invariant Feature Transform (SIFT), Enhanced Correlation Coefficient-based (ECC) with an affine transformation, and ECC with a homography transformation (Lowe 1999; Evangelidis and Psarakis 2008;

Alcantarilla *et al.* 2012). To generate the transformation matrix of images, we used an iterative method that compares image *i* to image *i+1*. A transformation matrix is then applied to each respective image after a buffer has been calculated, shifting images based on their transformation to maintain the true ground position *x,y*. The KAZE and SIFT algorithms use a Random Sample Consensus algorithm to generate a homography transformation. Additionally, we tested an affine and a homography transformation for the ECC algorithm. Affine transformations preserve parallel lines and ratio of distances, but a homography transformation is more adaptive to perspective shifts, such the vertical and horizontal drift of a UAS. We used a sample thermal image stack (Hundred Rx plot 2) to test each transformation algorithm. With ~9,000 infrared images, manual georectification was not possible. Therefore, to evaluate the transformation models, we manually selected the location of the ground control points (GCPs) of 30 images to compare to the first image of the image stack. Then, the positional distance of selected pixels from reference pixels was calculated as:

Equation S2

$$d(p_1, p_2) = \sqrt{(p_{1x} - p_{2x})^2 + \left(p_{1y} - p_{2y}\right)^2}$$

where $d(p_1,p_2)$ is the Euclidian distance between points p_1 and p_2 and each point is broken down into their respective x and y pixel coordinates. We used the ECC model with an affine transformation to stabilize all thermal imagery hereafter.

Using Hanna Hammock plot two imagery, we tested the performance of stabilization models and a fire/no-fire mask for removing positional and rotational drift from the thermal

image stacks (Fig. S2). The SIFT algorithm with a fire pixel mask performed the best, stabilizing the image stack with a median Euclidian error (Equation S1) of 3.5 pixels (SD = 1.1). Nonetheless, we used the second-best performing stabilization model, the ECC-affine transformation (median = 11.1, SD = 3.4), to stabilize all the plots for analysis because it was notably more robust to large changes between images, such as perspective shifts from interruptions in sampling for battery replacements, wind, and rapid fire growth. All plots were processed with the ECC-affine stabilization model with no mask for further analysis.

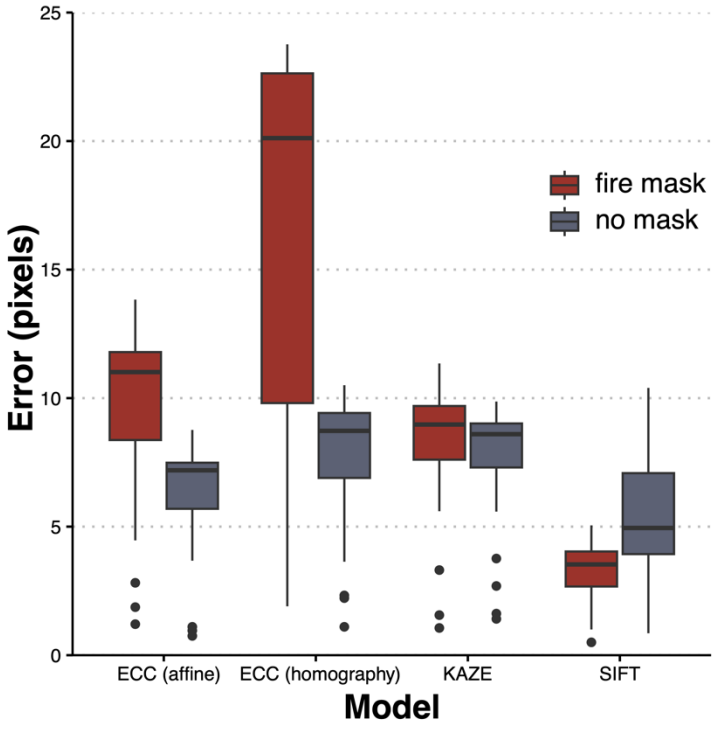

Figure S2: Error of the stabilization models tested: Enhanced Correlation Coefficient (ECC) with an affine transformation, ECC with a homography transformation, KAZE, and Scale Invariant Feature Transform (SIFT). Each model was tested with and without a mask that removed flaming areas. Error was measured using the Euclidian distance (Equation S2) of GCPs of image

i relative to the first image (reference image) in 30 selected images from the stabilized image stack, expressed in pixels with a mean resolution of 12 cm.

After image stabilization was complete, we georeferenced the image stacks using the locations of four GCPs visible in the thermal images (GDAL/OGR Contributors 2023). Transform matrices were generated manually for the first images and applied to all the stabilized images. If the plot was sampled for more than an hour or there was a visible shift or distortion in the stabilization process, the images were divided into sub-stacks, the first image was georeferenced, and the sub-stacks were remerged. To validate the final result of the stabilization and georeferencing process, we selected 30 images from each plot image stack incrementally, representing the entire duration of the image stack. Then, we manually identified visible GCPs in each image. The coordinate location of each selected point was compared to the true location of the nearest GCP using Equation S1 to calculate the distance error after processing (Fig. S3). The Root Mean Squared Error (RMSE) was calculated for each plot using the average distance error (Equation S2) of each of the thirty images sampled.

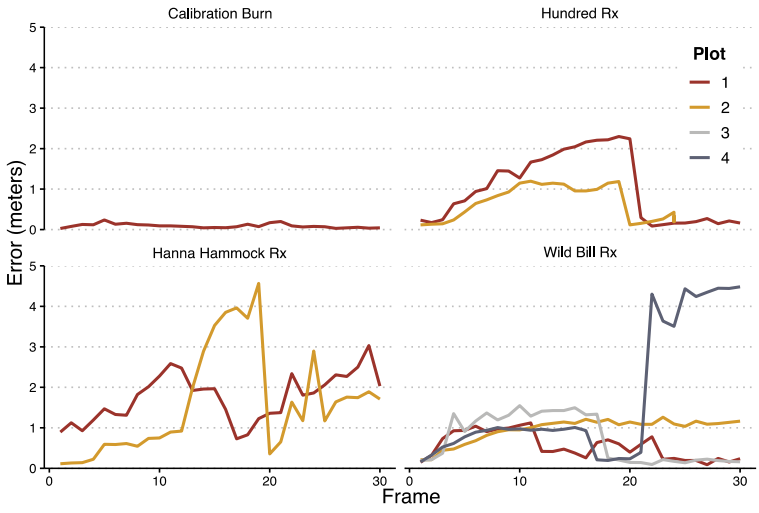

Figure S3: Final stabilization results after georeferencing. While most thermal image stacks had less than two m of positional error relative to the ground control points, instances of significant positional drift were present in some image stacks.

Once the images were georectified and converted to temperature, we processed the image stack from temperature to measurements of energy and power. To do this, we converted the radiant temperature of each pixel to fire radiative power (FRP; W m^{-2}) using the Stephan-Boltzmann law for grey body emitters, applied similarly in Hudak et al. (2018):

Equation S3

$$FRP = \epsilon\sigma(\mathrm{T_i}^4 - T_{bi}^4)$$

where ϵ is the emissivity of the grey body, σ is the Stephan-Boltzmann constant ($5.67*10^{-8}$ W m^{-2} K^{-4}), T is radiant temperature (Kelvin), and T_b is the background temperature (Kelvin). We used an emissivity constant of 0.98 (López *et al.* 2012; O'Brien *et al.* 2015; Moran *et al.* 2019). We elected to use a background temperature equal to the 10^{th} percentile of pixel temperatures for each raster image. The background temperature (T_b) accounts for changes in surface temperatures from solar radiation during multi-hour IR image collection. The 10^{th} percentile background temperatures were often near 300° K, the background temperature used by Hudak et al. (2018).

We approximately integrated pixel-scale measurements of FRP to calculate fire radiative energy (FRE; MJ m^{-2}) using the trapezoidal rule (Hudak *et al.* 2016, 2018), effectively converting power to energy:

Equation S4

$$FRE \approx \frac{1}{2}\sum_{i=1}^{n}(\mathrm{FRP_i} + \mathrm{FRP_{i-1}}) \cdot (\mathrm{t_i} - t_{i-1})$$

where consecutive FRP rasters are integrated over time, *t* (seconds). We used the trapezoidal rule because some image stacks had pauses in collection (i.e., swapping UAS batteries). Images were sampled every five seconds but there were some breaks in data collection when batteries were exchanged or, in the case of two plots, periods when there was little change in fire spread or energy release.

Canopy cover, where present, occluded nearly all the thermal radiation from surface fuel consumption below the canopy. We removed the sub-canopy FRP pixels by masking any pixels that did not reach a radiative power of 1,070 W m^{-2}, which was visually comparable to canopy cover of the plots (Hudak *et al.* 2016). To correct for the observational bias resulting from canopy cover occlusion, we use the un-masked area of the plot to calculate final estimates of consumption. For example, if a 1 ha plot has 20% canopy cover, then ~20% of the area was masked and fuel consumption estimates were multiplied by the proportional masked area (1.2), similar to Hudak et al. (2016).

S2: Hanna Hammock prescribed fire objectives. From correspondence with Tall Timbers Research Station.

From Eric Staller, Tall Timbers land manager, September 5th, 2023: "My objectives for TT burns are 95% fuel reduction and hardwood top kill. Limbing of pines less than 20 feet tall, and pushing fire deeper to drains and wetlands."

S3: Hundred prescribed fire objectives. From Tonto National Forest 2023 Burn Plan.

Resource objectives: This project is consistent with direction found in the Tonto Land Management Plan for area 5D and 5G. The project area is within Management Area 5D and 5G identified in the Tonto Forest Plan (USDA, 1985, as amended). Management emphasis for this area is to manage for a variety of renewable natural resources with primary emphasis on wildlife habitat, livestock forage and dispersed recreation. Watersheds are managed to meet satisfactory condition. Use prescribed fire to treat vegetation for water yield, forage, and wildlife habitat improvement. The overall intent will be to burn 375 to 15,000 acres per year to reduce the threat of negative impacts to watershed functions including erosion, and reduction in herbaceous productivity.

> Project falls within Categorical Exclusion category 32.2 (6) Timber stand and/or wildlife habitat improvement activities that do not include the use of herbicides or do not require more than 1 mile of low standard road construction. (IV). Prescribed burning to reduce natural fuel build-up and improve plant vigor.

Prescribed fire objectives: Initial entry burns will use backing fire and strip head fire in ponderosa pine and pinyon/juniper stands to reduce dead and down fuel loadings from 15-20 tons per acre to 10-15 tons per acre. Reduce the under-story vegetation by 75 - 90 percent. Reduce activity slash up to 80 percent. Reduce the over story by no more than 20 percent.

For maintenance burning in ponderosa pine reduce dead and down fuel loadings to 5-7 tons per acre. Reduce the under-story vegetation by 35-90 percent. Reduce the over-story by no more than 15 percent.

In continuous chaparral fuel stands use head fire to reduce the over story density by 50 - 80 percent. Achieve a mosaic burn pattern to create a range of age classes in brush stands. Promote herbaceous species growth by creating openings from 1 - 40 acres in size in accordance with the forest plan.

Objectives should be completed post burn and will be analyzed observationally within the first year.

Desired Effects:

Range of Acceptable Results, Expressed in quantifiable terms:
Ponderosa Pine / Pinyon/Juniper (this will be achieved with first entry and maintenance prescribed burning)

- Reduce Time Lag fuel loadings, 1, 10,100, and 1000 hour by 50% - 85%.
- Reduce under story 35% - 90%.

- Retain a minimum of one snag per acre where applicable.
- Retain 75% - 100% of the desirable trees.

Chaparral Burning

- Reduce over story density by 50% - 80%.
- Create openings of 1 to 200 acres in size with the goal of creating a variety of age class regeneration.
- Achieve a mosaic burn pattern by varied ignition patterns.
- Reduce 1- and 10-hour time lag fuels by 1 - 5 tons per acre.

S4: Wild Bill prescribed fire objectives. From Wild Bill incident action plan.

This Burn Plan supports retaining:

- 2 snags per acre, greater than or equal to 30 feet high and 18-inch diameter breast height.
- 3 logs per acre greater than or equal to 12-inch at mid-point.
- 5 to 7 tons of coarse woody debris per acre in the ponderosa pine ecosystem.
- Openings may be up to 4 acres with a maximum width of 200’.
- In the pinyon-juniper cover type, snags would be managed for one per acre over 75% of the area and coarse woody debris of 1-3 tons per acre.
- To minimize the potential for crown fire initiation, the desired condition is to have the average stand canopy base height above 18 feet (currently at 16').

- Presently the existing potential for crown fire is 38% through the 4FRI analysis area, and the desired condition is to be at no more than 10%.
- High severity fire should occur on no more than 10% of the treatment area (see below for severity definition).

S5: Prescribed fire visual observations

We visually observed low severity fire consuming ground and surface fuels at each of the prescribed fires. Of the fires, the Hanna Hammock Rx had the highest observed intensity with a few instances of crown scorching, high rates of spread (> 8 m min^{-1} at peak), and head fire with flame lengths up to 1 m. We observed lower intensities at the Hundred Rx and Wild Bill Rx: rates of spread (< 2 m min^{-1}) and fire front flame lengths (< 0.5 m) were low with the fire backing and flanking while consuming coarse woody debris. Post-frontal residence time (> 30 min) was longer and fuel consumption was higher at Wild Bill and Hundred burns as many of the plots had large amounts of coarse woody debris present. Much of the fuel at Hanna Hammock was fine (litter, shrubs, and small sticks), so post-frontal combustion was on the order of minutes rather than hours like the burns in Arizona.

Supplementary references

Alcantarilla PF, Bartoli A, Davison AJ (2012) KAZE Features. In “Computer Vision,” 214–227 doi:10.1007/978-3-642-33783-3_16.

Bradski G (2000) The OpenCV Library.

Evangelidis GD, Psarakis EZ (2008) Parametric image alignment using enhanced correlation coefficient maximization. *IEEE Transactions on Pattern Analysis and Machine Intelligence* **30**, 1858–1865. doi:10.1109/TPAMI.2008.113.

GDAL/OGR Contributors (2023) GDAL/OGR Geospatial Data Abstraction software Library. doi:10.5281/zenodo.5884351.

Hudak AT, Dickinson B MB, Bright BC, Kremens RL, Loudermilk EL, O'brien JJ, Hornsby BS, Ottmar RD (2016) Measurements relating fire radiative energy density and surface fuel consumption - RxCADRE 2011 and 2012. *International Journal of Wildland Fire* **25**,. doi:10.1071/WF14159.

Hudak AT, Freeborn PH, Lewis SA, Hood SM, Smith HY, Hardy CC, Kremens RJ, Butler BW, Teske C, Tissell RG, Queen LP, Nordgren BL, Bright BC, Morgan P, Riggan PJ, Macholz L, Lentile LB, Riddering JP, Mathews EE (2018) The cooney ridge fire experiment: An early operation to relate pre-, active, and post-fire field and remotely sensed measurements. *Fire* **1**, 1–32. doi:10.3390/fire1010010.

López A, Molina-Aiz FD, Valera DL, Peña A (2012) Determining the emissivity of the leaves of nine horticultural crops by means of infrared thermography. *Scientia Horticulturae* **137**, 49–58. doi:10.1016/j.scienta.2012.01.022.

Lowe DG (1999) Object recognition from local scale-invariant features. *Proceedings of the IEEE International Conference on Computer Vision* **2**, 1150–1157. doi:10.1109/ICCV.1999.790410.

Mahesh, Subramanyam M V. (2012) Automatic feature based image registration using SIFT algorithm. In "2012 Third International Conference on Computing, Communication and

Networking Technologies (ICCCNT'12)," 1–5. (IEEE) doi:10.1109/ICCCNT.2012.6396024.

Moran CJ, Seielstad CA, Cunningham MR, Hoff V, Parsons RA, Queen L, Sauerbrey K, Wallace T (2019) Deriving fire behavior metrics from UAS imagery. *Fire* **2**, 1–20. doi:10.3390/fire2020036.

O'Brien JJ, Loudermilk EL, Hornsby B, Hudak AT, Bright BC, Dickinson MB, Hiers JK, Teske C, Ottmar RD, O'Brien JJ, Loudermilk EL, Hornsby B, Hudak AT, Bright BC, Dickinson MB, Hiers JK, Teske C, Ottmar RD (2015) High-resolution infrared thermography for capturing wildland fire behaviour: RxCADRE 2012. *International Journal of Wildland Fire* **25**, 62–75. doi:10.1071/WF14165.

Paugam R, Wooster MJ, Mell WE, Rochoux MC, Filippi J-B, Rücker G, Frauenberger O, Lorenz E, Schroeder W, Main B, Govender N (2021) Orthorectification of Helicopter-Borne High Resolution Experimental Burn Observation from Infra Red Handheld Imagers. *Remote Sensing* **13**, 4913. doi:10.3390/rs13234913.

Valero MM, Verstockt S, Butler B, Jimenez D, Rios O, Mata C, Queen Ll, Pastor E, Planas E (2021) Thermal infrared video stabilization for aerial monitoring of active wildfires. *IEEE Journal of Selected Topics in Applied Earth Observations and Remote Sensing* **14**, 2817–2832. doi:10.1109/JSTARS.2021.3059054.